SURFACE MODIFICATION OF MAGNETIC TIO2 CORE-SHELL WITH DOPED CERIUM FOR ENHANCEMENT OF PHOTOCATALYTIC PERFORMANCE

Структура ядро-оболонка легованого Ce TiO₂@SiO₂@(Ni-Cu-Zn) фериту, зазначеного як CTSF у вигляді композитних наночастинок (НЧ), була синтезована з використанням модифікованого золь-гель методу. Фізико-хімічні властивості отриманих продуктів були повністю охарактеризовані за допомогою рентгенівської дифракції (РД), методу Брунауера-Еммета-Теллера (БЕТ), рентгенівської фотоелектронної спектроскопії (РФЕС) і надпровідного квантового інтерференційного пристрою (СКВІД). Тим часом оцінювання фотокаталітичної активності каталізатора проводили методом спектроскопії у видимій та ультрафіолетовій областях (УФ-вид). Результати дослідження показують, що анатазна фаза, пов'язана зі структурою TiO₂, була побудована на зовнішній оболонці композитних НЧ. Однак другу фазу, пов'язану зі структурою Ce, було нелегко виявити на рентгенограмі, що підтвердило включення легованого Ce в кристалічну структуру TiO₂. Мезопориста структура легованих Ce шарів TiO₂ була продемонстрована за допомогою ізотерми типу IV і петлі гістерезису типу H3. Був сформований однорідний розмір пор при питомій площі поверхні до 111,916 м²/г і 0,241 см³/г об'єму пор. Стехіометрія хімічного складу, утвореного з меншою кількістю дефектів на поверхні шарів TiO₂, продемонстрована кривою симетрії піків Ti 2p₃/₂ та Ti 2p₁/₂ РФЕС-спектрів. Тим часом окислювально-відновна пара, що відповідає Ce³⁺/Ce⁴⁺, була включена в тонке покриття TiO₂. Крім того, каталітичні магнітні НЧ також можуть бути відокремлені з використанням зовнішнього магнітного поля від реакційної системи. Характеристики продукту, пов'язані з ефективністю розкладання, досягли 50 % у водному розчині метиленового синього (МС)

Ключові слова: магнітний фотокаталізатор, фотодеградація, легований церієм TiO₂, поверхнева модифікація, фотокаталітичні характеристики

Fachruddin
Master of Engineering *
E-mail: fachruddin@mesin.pnj.ac.id
Iwan Susanto
Doctor of Materials Science and Engineering,
Assistance Professor*
E-mail: iwan.susanto@mesin.pnj.ac.id
Ching-Cheng Chen
Doctor of Materials Science and Engineering
Department of Materials Science and Engineering
National Dong Hwa University
Shoufeng Township, Hualien 97401, Taiwan ROC
E-mail: 810022002@ems.ndhu.edu.tw
Nugroho Eko Setijogiarto
Master of Engineering *
E-mail: nugrohoeko156@gmail.com
Fuad Zainuri
Doctoral Candidate of Mechanical Engineering *
E-mail: fuad.zainuri@mesin.pnj.ac.id
Sulaksana Permana
Doctor of Engineering in Metallurgy and Materials **
E-mail: sulaksana@yahoo.com
Johny Wahyuadi Soedarsono
Doctor of Engineering, Professor**
E-mail: jwsono@metal.ui.ac.id
*Department of Mechanical Engineering
State Polytechnic of Jakarta
Depok 16424, Jawa Barat, Indonesia
**Centre of Mineral Processing and Corrosion Research
Department of Metallurgy and Materials
Universitas Indonesia
Depok 16424, Jawa Barat, Indonesia

1. Introduction

As industrialization and globalization continue to develop, environmental problems caused by organic contaminants and energy crises are a serious concern [1, 2]. Semiconductor photocatalysts are a proven technology for environmental purification, especially liquid waste through the degradation of pollutants by utilizing solar energy into chemical energy [3, 4]. Up to now, some semiconducting nanocatalysts, namely ZnO, TiO₂, WO₃, ZnS, CdS, and Fe₂O₃, etc. were used continually for the abstraction of organic effluents from industrial wastewater [5–7]. Particularly, TiO₂ is an attrac-

tive semiconductor material that has been widely utilized in this system because of its superior photoelectric properties, non-toxicity, low cost and high stability [8–11]. In the working mechanism of the TiO_2 system, the electrons in the upper valence band will jump into the conduction band as they received the ultraviolet light, generating the electron and holes pair [12]. They create the formation of reactive oxygen species, which play directly for the degradation of organic pollutants via oxidation process. However, the rapid recombination rate for charge-carrying of electron pair holes and the narrow range of light response become a serious problem, which inhibits the photocatalytic process in practical applications [13, 14]. In addition, the difficulty of separating the catalyst from the reaction system also leaves a new issue as they are applied in liquid waste treatment.

Several attempts have been made to overcome the issue by expanding the gap of the TiO_2 absorption band with reducing the possibility of recombination for electron-hole pairs. The strategies carried out include the design of sensitivity, doping impurities by the metal ions, and incorporation with other semiconductors [15–17]. In another part, the magnetic catalyst nanoparticles were also a good model to be developed for separating the catalyst product from the reaction system, which further will be described in more detail in the literature review. Thus, the collaboration between both the doping material and the magnetic catalyst model is an interesting strategy to be investigated in order to reduce the issue above.

2. Literature review and problem statement

Modification of TiO_2 catalyst by doping ions mechanism using the rare earth materials proven can enhance the photocatalytic activity [18]. Cerium (Ce) is one of the attractive rare earth materials that could prevent the electron-hole recombination rate in TiO_2 [19, 20]. The study reported that doping of Ce up to 1 % (w/w) in TiO_2 can increase the photocatalytic efficiency in the 4-chlorophenol dye to be optimum up to 86.6 % for 3h at doping of 0.6 % Ce. However, the positive effect is maintenance with the crystalline structure as the synthesis of TiO_2 products was prepared by the solvothermolysis method. Another study developed with hydrothermal technique reported that the incorporation of Ce of 0.01 gram/Nitrogen for TiO_2(0.01Ce/N-TiO_2) in the AO-7 dye increased the photocatalytic degradation up to 79.04 %, which was facilitated by the reduction of recombination rate of electron holes pair [21]. Likewise, the attending of Ce^{3+}/Ce^{4+} mixture in TiO_2 formed by the sol-gel process was an effective mode for inhibiting the electron-holes recombination, enhancing the photocatalytic activity [22]. The experiment of doping (0–2.0 %Ce)/La–TiO_2 demonstrated that product yields for 1.5 wt %Ce/La/TiO_2 were around 1.8, 1.9 and 2.1 times compared to La/TiO_2 for CH_3OH, CH_4 and CO. Several recent investigations also reported the superiority of cerium in doping TiO_2. A study of co-doped TiO_2 with 0.6 %Mn and 1 %Ce molar ratios exhibited the strongest photoactive catalyst with 94 % of DCF removal [23]. The cerium led to be an effective dopant for increasing the response of TiO_2 by an efficient bandgap narrowing and hindering the electron-hole recombination. Thus, it can improve the quantum yield in the photocatalytic process. In addition, an experimental result revealed that the doping model of 0.02 g Ce in TiO_2-NPs-AC at pH 5.0 has shown the higher concentration of BR 46 leading to a decrease in removal percentage [24]. Unfortunately for these catalysts model, failure to recycle these nanostructures not only increases processing costs but can also lead to new types of pollution.

For the reason, incorporation of magnetic materials with nano-based catalyst TiO_2 particles is of particular interest because of their unique magnetic response, chemically modified surface, and low toxicity [25–27]. The studies reported that the magnetic catalyst of TiO_2 composite could be recovered from the reaction solution by using a permanent magnet. However, the direct contact between the TiO_2 layer and magnetic component results in the negative effect, which facilitates the increasing rate in electron-hole recombination. For reducing the adverse influence of magnetic materials, the interface layer between the magnetic core and TiO_2 catalyst should be modified. Some works reported that using SiO_2 materials as an intermediate layer of the core-shell structure has been introduced for creating the magnetic catalyst of $TiO_2/SiO_2/$ ferrite [28–31]. So, the developing study of the magnetic catalyst by the intermediate layer is still promising in the TiO_2 core-shell structure.

In this study, surface modification of TiO_2 magnetic core-shell doped cerium as the catalyst product of Ce-doped $TiO_2@SiO_2@$(Ni-Cu-Zn) ferrite for enhancement of photocatalytic performance is reported. The doping composition of 2 %wt Ce in TiO_2 by the sol-gel method will be introduced. The characteristics of the structure, surface behavior and magnetic properties of the catalyst product are investigated and discussed in detail as well.

3. The aim and objectives of the study

The aim of the study is to improve the photocatalytic performance of the magnetic catalyst of the TiO_2 core-shell structure by adding cerium element.

To achieve this aim, the following objectives are accomplished:

– Synthesis of the catalyst magnetic nanoparticles (NPs) by the sol gel method to create the TiO_2 core-shell structure.

– Surface modification at the outermost layer of core-shell structure with doping cerium in TiO_2.

– Characterization of the structure, surface composition and magnetic properties of the product.

– Performance test of the product using the MB dye solution in a dark condition and under visible light.

4. Materials and methods for surface modification of TiO_2 magnetic core-shell structure doped cerium

4. 1. Catalyst synthesis

The applied procedure for the NPs synthesis of Ce-$TiO_2@SiO_2@$(Ni-Cu-Zn) ferrite magnetic photocatalyst noted as CTSF is schematically designed in the core-shell model. The detailed synthesis process was reported in our previous study [32]. The final model of CTSF was created from tetrabutlytitanate $(Ti(OC_4H_9)_4)$ doped with 2wt %Ce, for which is coated on the $SiO_2@$Ni-Cu-Zn fer-

rite (SF) nanoparticles. Further, the model was calcined at 500 °C for 3 hours to generate the anatase phase of TiO_2. All of the samples including (Ni-Cu-Zn) ferrite, SiO_2@(Ni-Cu-Zn) ferrite, TiO_2@SiO_2@(Ni-Cu-Zn) ferrite, and Ce-TiO_2@SiO_2@(Ni-Cu-Zn) ferrite were noted as F, SF, TSF, and 20CTSF, respectively. The samples are further characterized and tested to get the surface structure properties and photocatalystic performance.

4. 2. Catalyst characterization

The crystalline structure was observed by using the X-ray diffraction (XRD) with Cu K_α radiation (λ=0.154056 nm) (Rigaku D/Max-II, Tokyo, Japan) for a scan rate of 3°/minutes.The surface characteristics related to the surface area, pore volume, and pore size were measured by Brunauer–Emmit–Teller (BET) using nitrogen adsorption employing Autosorb-1C instrument (Quanta Chrome, Boynton Beach, FL). The nitrogen gas was used as an adsorbent, while pore volume and pore size were calculated from the BJH method cumulative adsorption. The surface chemical composition related to Ce element doped on the TiO_2 was measured by the X-ray photoelectron spectroscopy (XPS; VGS Thermo K-Alpha, Waltham, MA, USA) with an Al K_α radiation as the exciting source. The magnetization properties were performed at ambient temperature using the superconducting quantum interference device (MPMS5; Quantum Design, San Diego, CA) set-up with a maximum magnetic field of 10 kOe.

4. 3. Photocatalytic activity

The photo-degradation of MB concentration was carried out at 0.30 g powders of both TSF and 20CTSF magnetic photocatalysts in the 50 mL of 10 mg/L MB aqueous solution using UV–VIS spectrometer (Evolution 220; Thermo, Waltham, MA). Before the UV illumination process, the suspension was stirred with ultrasonic vibration in the dark room for 30 min to reach adsorption–desorption equilibrium. The performance of TSF and 20CTSF composite was measured under the 35-W Xe arc lamp acting as simulated sunlight for irradiation function. 5 mL of suspension was taken every 1 h during 6 h and centrifuged for separate powders with reacting liquid prior which was analyzed based on the absorbance intensity of MB at 664.6 nm.

5. Experiment results of characterization of structure layer, surface area, surface composition, magnetic properties and photocatalytic performance

5. 1. XRD characterization

Fig. 1 shows the XRD pattern of photocatalyst nanoparticles for F, SF, and TSF samples. The ferrite phase includes both of the Ni-Zn and Fe_2O_3 associates of the core NPs shown in Fig. 1, *a* while the pattern of the SiO_2 coating is displayed in Fig. 1, *c*. Finally, Fig. 1, *c*, *d* demonstrates the pattern of anatase TiO_2 and Ce doped TiO_2 layer, serially.

Based on the XRD results in Fig. 1, there are two main peaks pattern raised with both Fe_2O_3 (□) and Ni-Zn ferrite (○) phase in Fig. 1, *a*. Both peaks initiate from the core of magnetic ferrite NPs. While the same peaks in Fig. 1, *b* are obtained due to the amorphous phase of the SiO_2 layer on the magnetic ferrite core NPs. In Fig. 1, *c*, the third phase with

the reduction in the intensity of both peaks before attend as the new peak of anatase (∇) from the TiO_2 structure. Meanwhile, there is no change of the pattern in Fig. 1, *d* with doped element Ce.
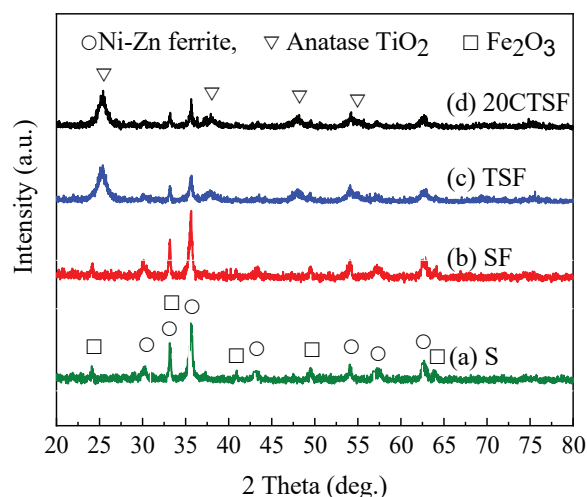

Fig. 1. XRD pattern of magnetic catalyst NPs of the sample: *a* — F, *b* — SF, *c* — TSF, and *d* — 20CTSF

5. 2. BET Analysis

Fig. 2, *a* displays the BET analysis results for isothermal adsorption-desorption of magnetic catalyst NPs of *a* – F; *b* – SF; *c* – TSF and *d* – 20CTSF, regularly. While BJH pore size distribution of nanoparticles photocatalyst is shown in Fig. 2, *b*. Besides, the surface area, pore diameter and pore volume of the magnetic catalyst NPs are tabulated in detail in Table 1.

On the BET curve results, the same trend with a narrow hysteresis loop with low pore volume both of F and SF samples were shown in Fig. 2, *a*. The broader hysteresis loop by higher pore volume was demonstrated by two kinds of the TSF and 20CTSF sample. For the BJH pore size distribution in Fig. 2, *b* the shaper peak of TSF compared to the 20CTSF sample was introduced. However, in the F and SF sample demonstrated the broader peak with low pore volume adsorbed.

Table 1

Pore characteristics of NPs photocatalyst

Sample	Surface Area S_{BET} (m^2/g)	Pore Diameter (Å)	Pore Volume (cc/g)
F	7.586	15.949	0.022
SF	7.395	15.902	0.018
TSF	126.831	26.457	0.244
20CTSF	111.916	30.763	0.241

Table 1 displays the surface characteristics of catalyst NPs associated with surface area, pore diameter, and pore volume, serially. The first column is the product sample. The second column is the surface area value that is the higher the S_{BET} value, the greater the surface area formed. Interim, the third column is the value of pore diameter created on the surface product. In the end column, it is the value of pore volume obtained from the accumulation of the pore diameter with the depth hollow constructed on the surface.
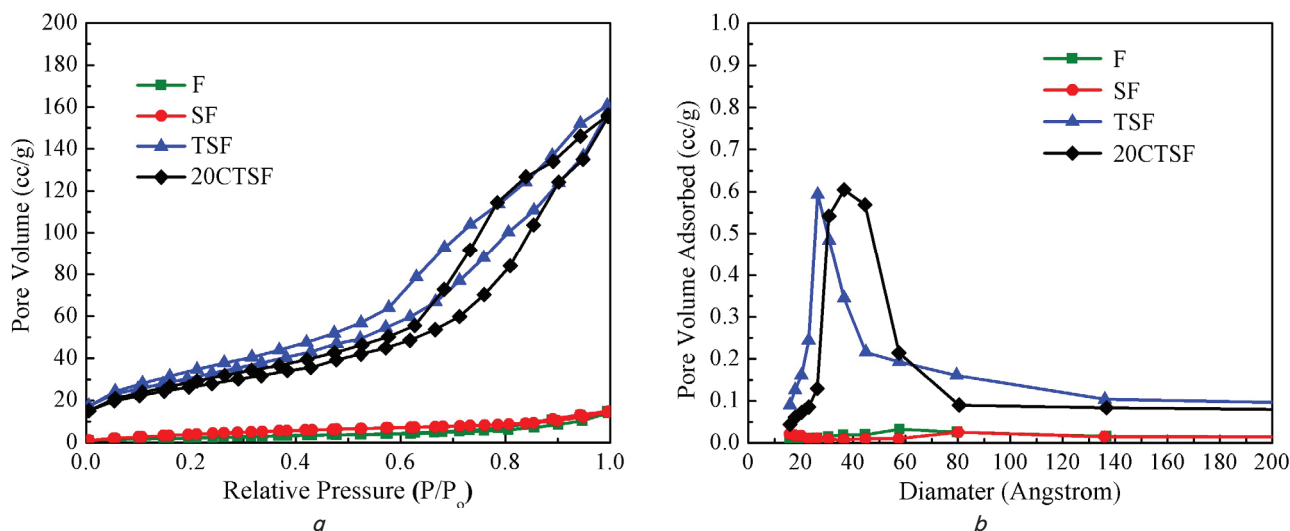
Fig. 2. N₂ adsorption-desorption isothermal of NPs photocatalyst: a — BET analysis using nitrogen gas for isothermal adsorption-desorption, b — BJH pore size distribution of NPs photocatalyst

5. 3. XPS Spectra

Fig. 3 presents completely the XPS spectra of surface composition for Ce-TiO₂/SiO₂/Ni-Cu-Zn. The full range of observation for all of the elements is shown in Fig. 3, a. The characteristics of Ti 2p peak and the bonding element of Ti-O were shown in Fig. 3, b, c, respectively. Furthermore, the Ce 3d spectrum compared to the TSF sample was exhibited in Fig. 3, d.

According to the results of examination of XPS spectra, all of the elements were detected on the full range observa-

tion up to 1,200 binding energy shown in Fig. 3, a. The Ti 2p peak including Ti 2p$_{3/2}$ and Ti 2p$_{3/2}$ correlated with titanium element present in the investigation in more detail at the range 456 to 468 eV in Fig. 3, b. While, the Ti-O bonding related to titanium oxide in Fig. 3, c was monitored in the range of 526 to 536 eV. Moreover, the attending of two photo-peaks compared to TSF peak representing the element cerium consist of Ce^{3+} 3d (trivalent) and Ce^{4+} 3d (tetravalent) was obtained for the range of 880 to 905 eV in Fig. 3, d.
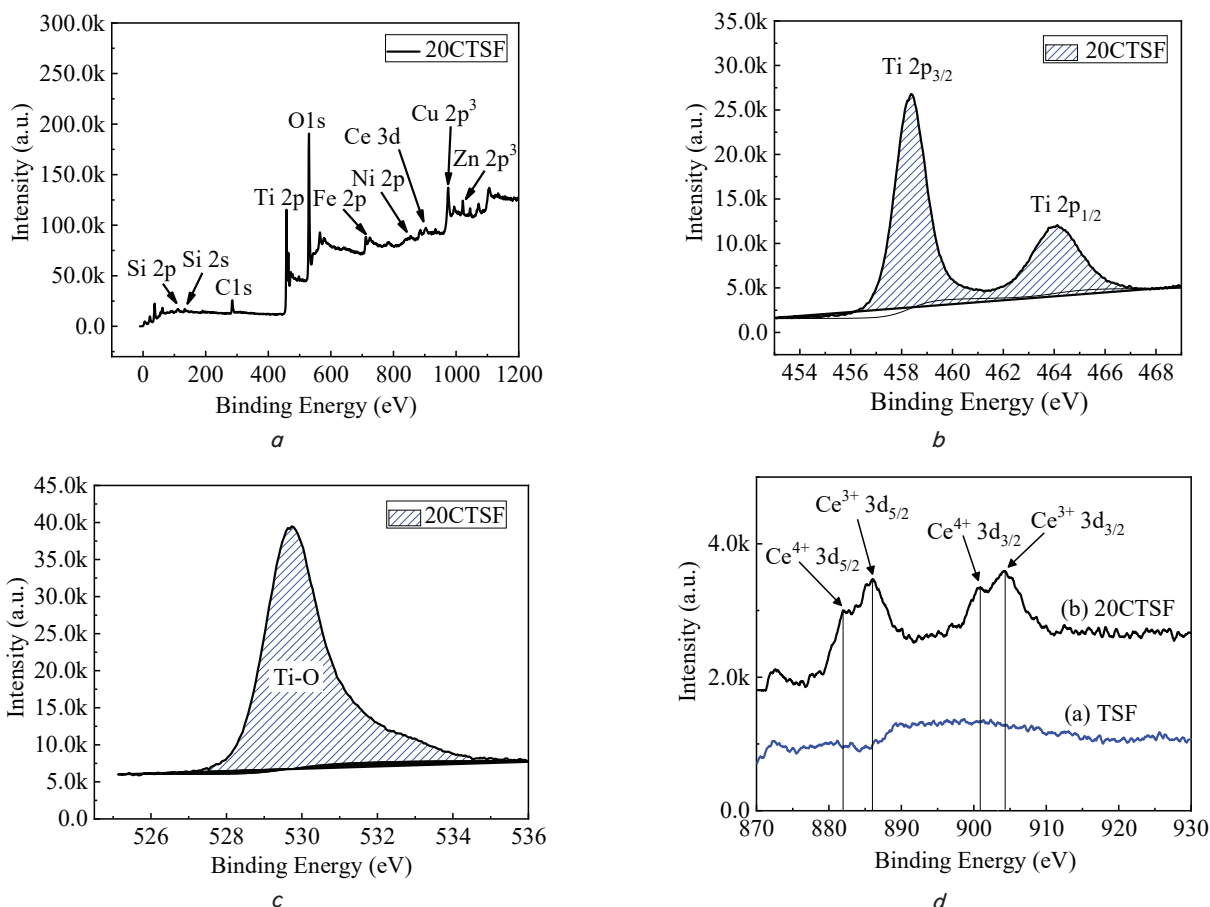

Fig. 3. XPS spectra of magnetic NPs on the 20CTSF layer: a — full range survey, b — characteristics of Ti 2p, c — oxygen incorporated in Ti; d — Ce 3d spectrum

5. 4. Magnetization Test

Fig. 4 provides the magnetic characteristics of all of catalyst NPs samples, which are performed by the superconducting quantum interference device at room temperature. The saturation magnetization value with the minimum hysteresis loop was shown in Fig. 4. The curve hysteresis loop of catalyst magnetic is noted as F, SF, TSF, and 20CTSF, regularly.

The magnetization curve of all catalyst products was shown in Fig. 4. The saturation magnetization values of F, SF, TSF, and 20CTSF samples are 28.12, 21.13, 4.73, and 9.23 emu/g, regularly. The greater value indicates the stronger performance of NPs for responding to the magnetic field. The inset of Fig. 4 demonstrates the photograph of 20CTSF NPs composite under a magnetic field after the completion of photo-degradation. The catalyst NPs can be collected from the deionized water solution after 30 seconds.
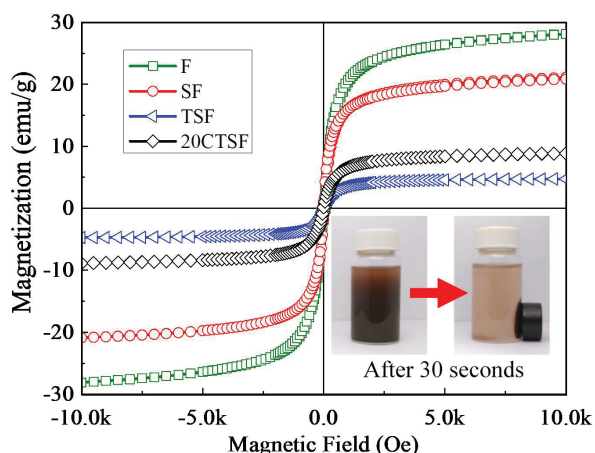

Fig. 4. Room-temperature magnetization curve of the products F, SF, TSF, and 20CTSF. The inset displays a photograph of the separation process in the product from the photocatalyst reaction

5. 6. Photodegradation Performance

Fig. 5 demonstrates the performance of magnetic catalyst NPs in MB dye solution, which is compared between both the TSF and 20CTSF samples. The catalytic activity was carried out in two steps, the first condition is in the dark room and the second phase is under visible light.
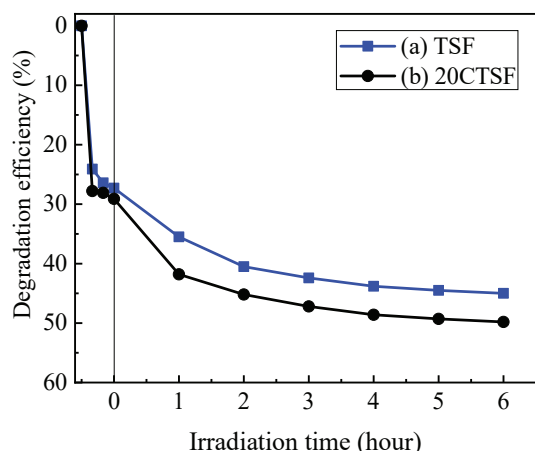

Fig. 5. Photodegradation of MB concentration for NPs catalyst as a function of irradiation time under visible light, as monitored by changes in the absorbance at 664.6 nm

Two curves were exhibited in Fig. 5 where the blue line and black one are associated with the degradation rate of MB dye solution with the catalyst NPs of TSF and 20CTSF, respectively. In the first step, the MB dye concentration was reduced up to 27 and 29 % for the TSF and 20CTSF solution. Further, for the second process, both curves go down continually as the irradiation time under visible light was added to the photodegradation system. The final reduction at 6 hours, the degradation efficiency was achieved at 45 and 50 % for both catalyst samples.

6. Discussion of experimental results

The XRD pattern of photocatalyst nanoparticles for F, SF and TSF samples was performed in detail shown in Fig. 1. The spinel crystal structure of particle ferrite (Ni-Cu-Zn) is demonstrated by the pattern of sample F in Fig. 1, *a*. The pattern matched with the Joint Committee of Powder Diffraction Standard (JCPDS) with the number of 08-0234 for the crystal structure of ferrite Ni-Zn [33]. However, there is a second phase attending in the pattern, which was also matched with JCPDS of 72-0469 for Fe_2O_3. Both kinds of those peak patterns seem broader, suggesting the particles in the nanometer size. After the deposited SiO_2 layer, there is no SiO_2 peak present on the pattern shown in Fig. 1, *b*. This could be due to the amorphous structure constructed on the SiO_2 layer. Since TiO_2 and Ce doped TiO_2 have coated on the SF particles, some of the new peaks attended on the XDR pattern in Fig. 1, *c*, *d*. Their presence was accompanied by a decrease in the intensity of some of the previous peaks. The new crystal peak located 25.27° at 2θ-XRD in (101) plane was originated from the anatase phase of TiO_2. The pattern is following JCPDS number 21-1272 for the anatase crystal structure of TiO_2 [34]. Based on the result, it is explained that the TiO_2 layer was successfully formed on the outer shell of composite nanoparticles of $TiO_2@SiO_2@$(Ni-Cu-Zn) ferrite. However, no peaks of Ce were detected on the pattern in Fig. 1, *d*, which confirmed that all of the doping Ce had been incorporated into the TiO_2 crystal structure.

The adsorption analysis of nitrogen gas was done for the characterization both of specific surface area and pore-size distribution of photocatalyst magnetic particles. Fig. 2, *a* displays nitrogen gas isothermal adsorption-desorption for samples F, SF, TSF, and 20CTSF, serially. The type IV isotherm and H3 type hysteresis loop were investigated for all samples, indicating the product of TSF and 20 CTSF having the mesoporous structure [35]. The specific surface area (SSA) of both models, calculated with the standard multi-points Brunauer-Emmett-Teller (BET) method, was obtained at 126.831 m^2g^{-1} and 111.916 m^2g^{-1}, respectively. However, for F and SF models, the SSA value was obtained lower than both models tabulated in detail in Table 1. Besides in Fig. 2, *b* the peak pore size distribution of TSF based on Barret-Joyner Halenda (BJH) desorption isotherm shows shaper than 20CTSF, suggesting a homogenous pore size in the sample [36]. The greater SSA might facilitate the more surface contact area, which could be beneficial for accelerating the photocatalyst reaction for reducing dyes molecules.

The surface chemical composition and bonding element of 20CTSF catalyst NPs were observed in more detail by XPS displayed in Fig. 3. The full range survey up to 1,200 eV for XPS spectra is shown in Fig. 3, *a*, which composite main peaks are Si 2p, 2s, C 1s, Ti 2p, O 1s, Fe$_2$ 2p, Ni 2p, Ce 3d, Cu 2p, and Zn 2p, serially. The attending of C 1s peak located at 285.1

related to carbon on the surface originates from the surface adventitious carbon. While the presence of Si 2p and Si 2s centered on 103 and 133.08 eV associate with the binding energy of Si^{4+} and O^{2-} in silica [37], identified due to the thin coating of TiO_2 on the SiO_2 layer. Meanwhile, the elements of Fe, Ni, Cu, and Zn corresponding to the magnetic core NPs are also detected at 709, 886, 975, and 1021 eV regularly, for which both layers of TiO_2 and SiO_2 are still in the very thin coating. Thus, the characteristic peaks of Ti 2p are demonstrated in detail in Fig. 3, *b*. There are two photo-peaks of Ti $2p_{3/2}$ and Ti $2p_{1/2}$ centered at 459.1 and 464.8 eV, serially [38]. The symmetry curve of both peaks without the shoulder on the lower energy sides indicates that the formation of TiO_2 was in the stoichiometries with fewer defects. Moreover, the O 1s peak binding energy with a prominent peak at 530 in Fig. 3, *c* was the oxygen incorporated in Ti, suggesting the Ti-O bonding constructed on the outer shell layers. Finally, the Ce 3d XPS spectrum peaks were identified in higher binding energy around 456 to 467 eV in Fig. 3, *d* [39], revealing that two photo-peaks of Ce^{3+} 3d (trivalent) and Ce^{4+} 3d (tetravalent) were attended for doping TiO_2. The centered peaks of the trivalent are in two peaks positions of 886.18 and 904.23 eV, while the tetravalent peaks are also in two locations of 882.63 and 901.08 eV regularly, suggesting the presence of a mixed-valence state for Ce ions in the TiO_2 layer.

Fig. 4 provides the magnetization curve of magnetic NPs tested at room temperature. The greater value indicates the stronger NPs influenced by a magnetic field. The magnetization curve of Ni-Cu-Zn ferrite as the catalyst core shows the minimal hysteresis loop ascribing a soft magnetic material of 28.12 emu/g compared to the bulk value of 80 emu/g. Furthermore, the decrease of saturation magnetization for SF TSF and 20CTSF corresponds to the nonmagnetic TiO_2 and SiO_2 layer coating over F NPs. The lower in these values is likely influenced by the thickness of the shell structure formed on the composite magnetic NPs. The inset of Fig. 4 demonstrates the photograph of 20CTSF NPs composite under a magnetic field after the completion of photo-degradation. It seems that the magnetic NPs of 20CTSF can be separated by using an external magnetic field for 30 seconds from the reaction system. The challenge of the model is to control the thickness of the layer as thin as possible during the synthesis process. The thinner layer coating can lead to the faster catalyst response to the external magnetic fields.

The photocatalystic activity of TSF and 20CTSF NPs was evaluated by the degradation of MB dye solution under visible light using a Xe arch lamp with 35 Watt in Fig. 5. Before photo-degradation under visible light, the adsorption-desorption was reacted in the dark room for 30 minutes whereas the decoloration of MB dye was achieved up to 27 and 29 % for TSF and 20CTSF NPs, respectively. It is well known that the surface area and many pores on the surface of catalyst NPs tabulated in Table 1 will facilitate the absorption of dyes contained in the MB solution. As the catalyst product was loaded under irradiation visible light, the photodegradation efficiencies were found to be increased gradually with increasing reaction time. The

enhancement of the degradation efficiency was achieved to be 45 and 50 % for catalyst NPs of TSF and 20CTSF for 6 hours. Higher efficiency for the 20CTSF catalyst was suggested that the redox couple Ce^{3+}/Ce^{4+} lead to reduced bandgap energy. It can also facilitate the effective recombination delay of photo-induced charge carriers [40]. Moreover, they also have an effective dopant for improving the response of TiO_2, which increases the quantum yield in the photocatalytic process [23]. However, the reduction of the specific surface area of 20CTSF based on the BET results can restrict the optimum performance of the product in degrading the MB dye. So, the right Ce doping composition is further needed to optimize the surface area for increasing the performance of the product. Also, the investigation related to the layer structure and surface morphology should be conducted in detail by the Transmission Electron Microscopy (TEM) and Scanning Electron Microscopy (SEM) to get a deep understanding of the character from the product. Thus, the cyclic loading should also be carried out to find out the performance of the product. Eventually, various dyes could be used to develop the product in the application.

7. Conclusions

1. The TiO_2 catalyst magnetic NPs as a synthesis product with the core-shell structure was successfully constructed by the sol gel method. The model of 2wt %Ce-TiO_2@SiO_2@ (Ni-Cu-Zn) ferrite noted as 20CTSF was introduced to the reduction of MB dye.

2. The attending of two photo-peaks of Ce^{3+} 3d (trivalent) and Ce^{4+} 3d (tetravalent) on the product layers was associated with the metal ions of Ce doping on the surface layer of TiO_2.

3. The anatase phase of the TiO_2 structure has formed on the outer layer of the core-shell structure. The large surface area and great pore volume have been achieved by the 20CTSF product up to 111.916 m^2/g and 0.241 cc/g, respectively. While the good enough magnetic field with 9.23 emu/g could separate the product by an external magnetic field from the reaction system.

4. The total performance of the 20CTSF product in the MB dye solution was achieved up to 50 % in the degradation efficiency during 6 hours. The performance of the catalyst was better up to 5 % of efficiency than without the doped Ce for the reduction of MB dye.

Acknowledgments

References

1. Lei, J., Wang, W., Song, M., Dong, B., Li, Z., Wang, C., Li, L. (2011). Ag/AgCl coated polyacrylonitrile nanofiber membranes: Synthesis and photocatalytic properties. Reactive and Functional Polymers, 71 (11), 1071–1076. doi: https://doi.org/10.1016/j.reactfunctpolym.2011.08.002

2. Zhang, J., Tian, B., Wang, L., Xing, M., Lei, J. (2018). Photocatalysis. Springer. doi: https://doi.org/10.1007/978-981-13-2113-9

3. Bavykin, D. V., Friedrich, J. M., Walsh, F. C. (2006). Protonated Titanates and TiO2 Nanostructured Materials: Synthesis, Properties, and Applications. Advanced Materials, 18 (21), 2807–2824. doi: https://doi.org/10.1002/adma.200502696

4. Zhang, Q., Lima, D. Q., Lee, I., Zaera, F., Chi, M., Yin, Y. (2011). A Highly Active Titanium Dioxide Based Visible-Light Photocatalyst with Nonmetal Doping and Plasmonic Metal Decoration. Angewandte Chemie International Edition, 50 (31), 7088–7092. doi: https://doi.org/10.1002/anie.201101969

5. Muersha, W., Pozan Soylu, G. S. (2018). Effects of metal oxide semiconductors on the photocatalytic degradation of 4-nitrophenol. Journal of Molecular Structure, 1174, 96–102. doi: https://doi.org/10.1016/j.molstruc.2018.07.034

6. Swaminathan, M. (2018). Semiconductor Oxide Nanomaterials as Catalysts for Multiple Applications. Handbook of Nanomaterials for Industrial Applications, 197–207. doi: https://doi.org/10.1016/b978-0-12-813351-4.00011-0

7. Ramchiary, A. (2020). Metal-oxide semiconductor photocatalysts for the degradation of organic contaminants. Handbook of Smart Photocatalytic Materials, 23–38. doi: https://doi.org/10.1016/b978-0-12-819049-4.00006-4

8. Li, R., Kobayashi, H., Guo, J., Fan, J. (2011). Visible-light-driven surface reconstruction of mesoporous TiO_2: toward visible-light absorption and enhanced photocatalytic activities. Chemical Communications, 47 (30), 8584. doi: https://doi.org/10.1039/c1cc12464a

9. Zhao, Y., Wang, Y., Xiao, G., Su, H. (2019). Fabrication of biomaterial/TiO_2 composite photocatalysts for the selective removal of trace environmental pollutants. Chinese Journal of Chemical Engineering, 27 (6), 1416–1428. doi: https://doi.org/10.1016/j.cjche.2019.02.003

10. Xing, Z., Zhang, J., Cui, J., Yin, J., Zhao, T., Kuang, J. et. al. (2018). Recent advances in floating TiO_2-based photocatalysts for environmental application. Applied Catalysis B: Environmental, 225, 452–467. doi: https://doi.org/10.1016/j.apcatb.2017.12.005

11. Wang, Y., Sun, C., Zhao, X., Cui, B., Zeng, Z., Wang, A. et. al. (2016). The Application of Nano-TiO2 Photo Semiconductors in Agriculture. Nanoscale Research Letters, 11 (1). doi: https://doi.org/10.1186/s11671-016-1721-1

12. Schneider, J., Matsuoka, M., Takeuchi, M., Zhang, J., Horiuchi, Y., Anpo, M., Bahnemann, D. W. (2014). Understanding TiO_2 Photocatalysis: Mechanisms and Materials. Chemical Reviews, 114 (19), 9919–9986. doi: https://doi.org/10.1021/cr5001892

13. Tan, L.-L., Chai, S.-P., Mohamed, A. R. (2012). Synthesis and Applications of Graphene-Based TiO2Photocatalysts. ChemSusChem, 5 (10), 1868–1882. doi: https://doi.org/10.1002/cssc.201200480

14. Ozawa, K., Emori, M., Yamamoto, S., Yukawa, R., Yamamoto, S., Hobara, R. et. al. (2014). Electron–Hole Recombination Time at TiO2 Single-Crystal Surfaces: Influence of Surface Band Bending. The Journal of Physical Chemistry Letters, 5 (11), 1953–1957. doi: https://doi.org/10.1021/jz500770c

15. Deshmane, V. G., Owen, S. L., Abrokwah, R. Y., Kuila, D. (2015). Mesoporous nanocrystalline TiO_2 supported metal (Cu, Co, Ni, Pd, Zn, and Sn) catalysts: Effect of metal-support interactions on steam reforming of methanol. Journal of Molecular Catalysis A: Chemical, 408, 202–213. doi: https://doi.org/10.1016/j.molcata.2015.07.023

16. Karafas, E. S., Romanias, M. N., Stefanopoulos, V., Binas, V., Zachopoulos, A., Kiriakidis, G., Papagiannakopoulos, P. (2019). Effect of metal doped and co-doped TiO2 photocatalysts oriented to degrade indoor/outdoor pollutants for air quality improvement. A kinetic and product study using acetaldehyde as probe molecule. Journal of Photochemistry and Photobiology A: Chemistry, 371, 255–263. doi: https://doi.org/10.1016/j.jphotochem.2018.11.023

17. Niu, M., Cheng, D., Cao, D. (2013). Enhanced photoelectrochemical performance of anatase TiO_2 by metal-assisted S−O coupling for water splitting. International Journal of Hydrogen Energy, 38 (3), 1251–1257. doi: https://doi.org/10.1016/j.ijhydene.2012.10.109

18. Štengl, V., Bakardjieva, S., Murafa, N. (2009). Preparation and photocatalytic activity of rare earth doped TiO_2 nanoparticles. Materials Chemistry and Physics, 114 (1), 217–226. doi: https://doi.org/10.1016/j.matchemphys.2008.09.025

19. Munir, B., Permana, S., Amilia, A., Maksum, A., Soedarsono, J. W. (2019). Initial Study for Cerium and Lanthanum Extraction from Bangka Tin Slag through NaOH and HClO4 Leaching. MATEC Web of Conferences, 269, 07003. doi: https://doi.org/10.1051/matecconf/201926907003

20. Silva, A. M. T., Silva, C. G., Dražić, G., Faria, J. L. (2009). Ce-doped TiO2 for photocatalytic degradation of chlorophenol. Catalysis Today, 144 (1-2), 13–18. doi: https://doi.org/10.1016/j.cattod.2009.02.022

21. Nasir, M., Bagwasi, S., Jiao, Y., Chen, F., Tian, B., Zhang, J. (2014). Characterization and activity of the Ce and N co-doped TiO_2 prepared through hydrothermal method. Chemical Engineering Journal, 236, 388–397. doi: https://doi.org/10.1016/j.cej.2013.09.095

22. Ali, K. A., Abdullah, A. Z., Mohamed, A. R. (2017). Visible light responsive TiO_2 nanoparticles modified using Ce and La for photocatalytic reduction of CO_2: Effect of Ce dopant content. Applied Catalysis A: General, 537, 111–120. doi: https://doi.org/10.1016/j.apcata.2017.03.022

23. Tbessi, I., Benito, M., Molins, E., LIorca, J., Touati, A., Sayadi, S., Najjar, W. (2019). Effect of Ce and Mn co-doping on photocatalytic performance of sol-gel TiO_2. Solid State Sciences, 88, 20–28. doi: https://doi.org/10.1016/j.solidstatesciences.2018.12.004

24. Alipanahpour Dil, E., Ghaedi, M., Asfaram, A., Mehrabi, F., Bazrafshan, A. A., Tayebi, L. (2019). Synthesis and application of Ce-doped TiO_2 nanoparticles loaded on activated carbon for ultrasound-assisted adsorption of Basic Red 46 dye. Ultrasonics Sonochemistry, 58, 104702. doi: https://doi.org/10.1016/j.ultsonch.2019.104702

25. Kim, H. S., Kim, D., Kwak, B. S., Han, G. B., Um, M.-H., Kang, M. (2014). Synthesis of magnetically separable core@shell structured NiFe2O4@TiO2 nanomaterial and its use for photocatalytic hydrogen production by methanol/water splitting. Chemical Engineering Journal, 243, 272–279. doi: https://doi.org/10.1016/j.cej.2013.12.046

26. Jing, J., Li, J., Feng, J., Li, W., Yu, W. W. (2013). Photodegradation of quinoline in water over magnetically separable Fe3O4/TiO2 composite photocatalysts. Chemical Engineering Journal, 219, 355–360. doi: https://doi.org/10.1016/j.cej.2012.12.058

27. Zhan, J., Zhang, H., Zhu, G. (2014). Magnetic photocatalysts of cenospheres coated with Fe3O4/TiO2 core/shell nanoparticles decorated with Ag nanopartilces. Ceramics International, 40 (6), 8547–8559. doi: https://doi.org/10.1016/j.ceramint.2014.01.069

28.   Mahesh, K. P. O., Kuo, D.-H. (2015). Synthesis of Ni nanoparticles decorated SiO2/TiO$_2$ magnetic spheres for enhanced pho-tocatalytic activity towards the degradation of azo dye. Applied Surface Science, 357, 433–438. doi: https://doi.org/10.1016/j.apsusc.2015.08.264

29.   MirzaHedayat, B., Noorisepehr, M., Dehghanifard, E., Esrafili, A., Norozi, R. (2018). Evaluation of photocatalytic degradation of 2,4-Dinitrophenol from synthetic wastewater using Fe3O4@SiO2@TiO2/rGO magnetic nanoparticles. Journal of Molecular Liquids, 264, 571–578. doi: https://doi.org/10.1016/j.molliq.2018.05.102

30.   Khodadadi, M., Ehrampoush, M. H., Ghaneian, M. T., Allahresani, A., Mahvi, A. H. (2018). Synthesis and characterizations of Fe-Ni$_3$@SiO$_2$@TiO$_2$ nanocomposite and its application in photo- catalytic degradation of tetracycline in simulated wastewater. Journal of Molecular Liquids, 255, 224–232. doi: https://doi.org/10.1016/j.molliq.2017.11.137

31.   Liu, Y., Cherkasov, N., Gao, P., Fernández, J., Lees, M. R., Rebrov, E. V. (2017). The enhancement of direct amide synthesis reaction rate over TiO$_2$@SiO$_2$@NiFe$_2$O$_4$ magnetic catalysts in the continuous flow under radiofrequency heating. Journal of Catalysis, 355, 120–130. doi: https://doi.org/10.1016/j.jcat.2017.09.010

32.   Chen, C.-C., Fu, Y.-P., Hu, S.-H. (2015). Characterizations of TiO$_2$/SiO$_2$/Ni-Cu-Zn Ferrite Composite for Magnetic Photocatalysts. Journal of the American Ceramic Society, 98 (9), 2803–2811. doi: https://doi.org/10.1111/jace.13685

33.   Chen, C.-C., Jaihindh, D., Hu, S.-H., Fu, Y.-P. (2017). Magnetic recyclable photocatalysts of Ni-Cu-Zn ferrite@SiO2@TiO2@Ag and their photocatalytic activities. Journal of Photochemistry and Photobiology A: Chemistry, 334, 74–85. doi: https://doi.org/10.1016/j.jphotochem.2016.11.005

34.   Zhu, L.-P., Huang, C., Liu, J.-W., Bing, N.-C., Jin, H.-Y., Wang, L.-J. (2013). Synthesis and characterization of cage-like core–shell structured TiO2 hollow microspheres. Materials Letters, 106, 348–351. doi: https://doi.org/10.1016/j.matlet.2013.05.093

35.   Chen, J., Lin, S., Yan, G., Yang, L., Chen, X. (2008). Preparation and its photocatalysis of Cd1−xZnxS nano-sized solid solution with PAMAM as a template. Catalysis Communications, 9 (1), 65–69. doi: https://doi.org/10.1016/j.catcom.2007.05.022

36.   Paquin, F., Rivnay, J., Salleo, A., Stingelin, N., Silva-Acuña, C. (2015). Multi-phase microstructures drive exciton dissociation in neat semicrystalline polymeric semiconductors. Journal of Materials Chemistry C, 3 (41), 10715–10722. doi: https://doi.org/10.1039/c5tc02043c

37.   Aghaei, R., Eshaghi, A. (2017). Optical and superhydrophilic properties of nanoporous silica-silica nanocomposite thin film. Journal of Alloys and Compounds, 699, 112–118. doi: https://doi.org/10.1016/j.jallcom.2016.12.327

38.   Karthick, S. N., Prabakar, K., Subramania, A., Hong, J.-T., Jang, J.-J., Kim, H.-J. (2011). Formation of anatase TiO$_2$ nanoparticles by simple polymer gel technique and their properties. Powder Technology, 205 (1-3), 36–41. doi: https://doi.org/10.1016/j.powtec.2010.08.061

39.   Zhan, F., Liu, W., Li, H., Yang, Y., Wang, M. (2018). Ce-doped CdS quantum dot sensitized TiO$_2$ nanorod films with enhanced visi-ble-light photoelectrochemical properties. Applied Surface Science, 455, 476–483. doi: https://doi.org/10.1016/j.apsusc.2018.05.226

40.   Yu, T., Tan, X., Zhao, L., Yin, Y., Chen, P., Wei, J. (2010). Characterization, activity and kinetics of a visible light driven photo-catalyst: Cerium and nitrogen co-doped TiO2 nanoparticles. Chemical Engineering Journal, 157 (1), 86–92. doi: https://doi.org/10.1016/j.cej.2009.10.051